OVERSHOOTING CONVECTION FROM HIGH-RESOLUTION NEXRAD OBSERVATIONS

A Thesis

by

DAVID LAURENCE SOLOMON

Submitted to the Office of Graduate and Professional Studies of
Texas A&M University
in partial fulfillment of the requirements for the degree of

MASTER OF SCIENCE

Chair of Committee,   Kenneth P. Bowman
Committee Members,   Andrew Dessler
   David Brooks
Head of Department,   Ping Yang

May 2014

Major Subject: Atmospheric Sciences

ABSTRACT

Convection can rapidly and irreversibly transport tropospheric air into the upper troposphere and, in some cases, through the tropopause into the lower stratosphere. Previous studies have shown that stratosphere-troposphere exchange of any kind can have a significant impact on the composition of the upper troposphere and lower stratosphere. This will in turn affect the climate, chemistry, and radiation budget of the atmosphere. Large scale transport events such as Rossby wave breaking, the Brewer-Dobson circulation, and tropopause folding have been well studied, but smaller-scale processes are less well understood. In order to understand the importance of convective transport on the composition of the lower stratosphere, it is necessary to know the frequency, magnitude, and location of overshooting convection events. A new method that combines radar reflectivities from individual radars into a three-dimensional composite with high vertical resolution is used to obtain storm top altitudes. These altitudes are compared to the lapse-rate tropopause height calculated using the ERA-Interim reanalysis to determine if a storm is overshooting. We compute a 1-year analysis of overshooting convection at three-hour intervals for 2004 for the continental U.S. east of the Rocky Mountains. Overshooting convection is most common over the high plains, and there is a pronounced seasonal and diurnal cycle present. The majority of overshooting systems occur during the warm season, and a diurnal maximum of overshooting occurs at 00 UTC. Analyzing the total volume of tropopause penetrating storms reveals that the largest amount of overshooting penetrates less than 1 km above the tropopause, and that the volume of overshooting drops off rapidly with increasing height above the tropopause.

TABLE OF CONTENTS

LIST OF FIGURES

iv

1. INTRODUCTION

Changes in the composition of the Upper Troposphere and Lower Stratosphere (UTLS) have been shown to have large impacts on the chemistry, climate, and radiation budget of the troposphere and stratosphere (*Holton et al.*, 1995; *Stohl et al.*, 2003; *Forster and Co-authors*, 2007; *Gettelman et al.*, 2011). Because the lifetimes of many trace constituents are long in the UTLS, transport is often the dominant factor affecting their distributions. Many previous studies focusing on Stratosphere-Troposphere Exchange (STE) have investigated large-scale processes such as Rossby wave breaking, the Brewer-Dobson circulation, and tropopause folding as pathways for transport across the tropopause. There is a relatively good understanding of the dynamics and chemistry of these large-scale processes, but transport by smaller-scale processes, including convection, has not been studied as extensively.

Deep convection occurs in many locations around the globe and has the potential to lift boundary layer and lower tropospheric air rapidly into the UTLS. This study focuses on assessing the importance of tropopause-penetrating convection on the composition of the lower stratosphere. Therefore, we are interested primarily in Troposphere-to-Stratosphere Transport (TST), following the nomenclature of *Stohl et al.* (2003). Studies of convection in the tropics have shown that convection does occur to the altitude of the tropopause, and it plays a role in determining the abundance of trace species there (*Alcala and Dessler*, 2002; *Gettelman et al.*, 2002; *Dessler*, 2002). Numerous studies have also shown evidence of convection affecting the extratropical UTLS (e.g., *Poulida et al.*, 1996; *Fischer et al.*, 2003; *Fromm and Servranckx*, 2003; *Hegglin et al.*, 2004; *Ray et al.*, 2004; *Hanisco et al.*, 2007; *Anderson et al.*, 2012). Many of these studies of STE focus on an individual convective

event or a series of convective events that occur during a field campaign.

More recently, explicit modeling simulations of extratropical convection and the transport associated with that convection have been done (e.g., *Gray*, 2003; *Wang*, 2003; *Mullendore et al.*, 2005; *Changon and Gray*, 2010; *Le and Gallus*, 2012). These modeling studies, and the observational studies mentioned above, show that deep convection has the ability to influence the composition of the lower stratosphere. Because many of these studies focus on the exploration of a small number of storms, they are useful for diagnosing the effects of convection on the UTLS, but they cannot quantify the regional or global impact of deep convection on the layer. Current global climate models do not resolve individual convective cells, and thus their total impact on the lower stratosphere through TST is difficult to assess.

Several studies have attempted to use satellite observations to quantify the frequency and location of deep convection that penetrates the tropopause with varying success. *Berendes et al.* (2008) use a combination of visible and near-IR texture and reflectance to objectively detect convection penetrating the tropopause. This technique performs well at times around solar noon, but it suffers at low solar zenith angles due to enhanced texture in the visible channel imagery during these times, and it cannot be used at night when continental convection typically reaches its maximum intensity (*Dai et al.*, 1999). *Lindsey and Grasso* (2008) and *Rosenfeld et al.* (2008) use near-IR reflectance and ice particle effective radius techniques to locate storms that have penetrated the tropopause, but their method suffers from some of the same diurnal cycle issues as above, making these techniques non ideal for a complete accounting of overshooting systems (*Bedka et al.*, 2010).

Other studies have used a technique which employs the difference between 6-7 μm water vapor absorption and $\sim$11 μm infrared window channel brightness temperature for overshooting convection detection (e.g., *Fritz and Laszlo*, 1993; *Ackerman*,

1996; *Schmetz et al.*, 1997; *Setvak et al.*, 2007; *Martin et al.*, 2008). This technique works because the lapse rate in the stratosphere is inverted, and temperatures increase with increasing height. Water vapor injected into the lower stratosphere by the overshooting storm emits at the warmer stratospheric temperature while the emissions in the infrared window channel come from the colder cloud top. The difference between these two sources can then be used to diagnose where overshooting is occurring. The difference threshold needed for overshoot detection with this method varies depending on the measuring platform used, stratospheric lapse rate, intensity of the updraft, and residence time of the water vapor in the stratosphere.

Bedka et al. (2010) use a combination of infrared window brightness temperature spatial gradients and Global Forecast system (GFS) 6-hour forecasts of tropopause temperature to perform a five year climatology of overshooting convection across the Eastern portion of the United States. This method provides a representation of total overshooting convection by locating "cold" pixels with infrared window brightness temperatures less than or equal to 215 K and identifies the corresponding tropopause temperatures at each location. The mean anvil temperature surrounding each pixel is then calculated and if the cold pixel is at least 6.5 K colder than the anvil it is considered to be overshooting. Once a pixel is identified a circle with a radius of 6 Km and centered on that point is searched to locate other brightness temperatures that are at least 50% colder than the surrounding anvil brightness temperature. Results of this method show the the largest number of overshooting occurrences occur across the southeastern United States and southern Great Plains. The biggest draw back to this method is that it does not explicitly quantify overshooting height above the troposphere. Using typical lapse rates of overshooting storms (*Negri*, 1982; *Adler et al.*, 1983) *Bedka et al.* (2010) estimate the pixels they identify as overshooting are at least ∼0.7 to ∼0.9 km above the surrounding anvil cloud. Recent use of space-

borne lidar and radar have been able to provide measurements of deep convection altitude (*Setvàk et al.*, 2013). These platforms suffer from low spatial and temporal coverage and therefore cannot be used to obtain a complete picture of overshooting convective systems.

In order to understand the overall importance of deep, tropopause-penetrating, convection on the lower stratosphere, this study introduces a new method for combining reflectivities from individual NEXRAD WSR88-D radar sites into a 3-dimensional composite with high vertical resolution to obtain storm top altitudes. These altitudes are then compared to tropopause heights calculated from the ERA-Interim reanalysis in order to determine the extent of penetration into the stratosphere. A 1-year analysis of overshooting convection at three-hour intervals for 2004 over the continental U.S. east of the Rocky Mountains is created in order to assess the frequency, magnitude, and location of overshooting convection events. Additionally the volume of tropospheric air transported into the stratosphere as a function of height above the tropopause is estimated.

2.   DATA

2.1   NEXRAD WSR-88D Data

Radar data for this study are obtained from the National Climatic Data Center (NCDC). NEXRAD WSR-88D radars (referred to as NEXRAD herein) produce a beam with an ∼10 cm wavelength. This wavelength allows for sampling of larger precipitating hydrometeors with acceptable attenuation in heavy rain, but largely misses smaller non-precipitating particles (such as cloud droplets). NEXRAD radars transmit a conical beam with an angular width of 0.95°. The nominal altitude of the beam increases with distance from the radar site due to the tilt of the radar and the curvature of the Earth. Due to varying atmospheric refractive properties, beam position errors also generally increase with distance from the radar. Figure 2.1 shows the siting locations and coverage area below 10,000 feet for the NEXRAD radar network. NEXRAD radar locations were chosen to ensure sampling of the network was best over densely populated areas (*Leone et al.*, 1989). Because of these siting guidelines, coverage density generally decreases as you move west. For this study we use only radar sites located east of the Rocky Mountains.

NEXRAD radars directly measure three variables: reflectivity, radial velocity, and spectrum width, which are known collectively as Level 2 products. This study uses Level 2 reflectivity data to determine echo-top altitude. The radar data are stored at a resolution of 1° in azimuth and 1 km in radial distance on spherical grids for each radar. Tilt angles depend on the scanning mode in operation at a radar at a given time.

The sampling resolution at individual radar sites depends on several conditions including: operating status, scan strategy, range of the target volume from the radar,

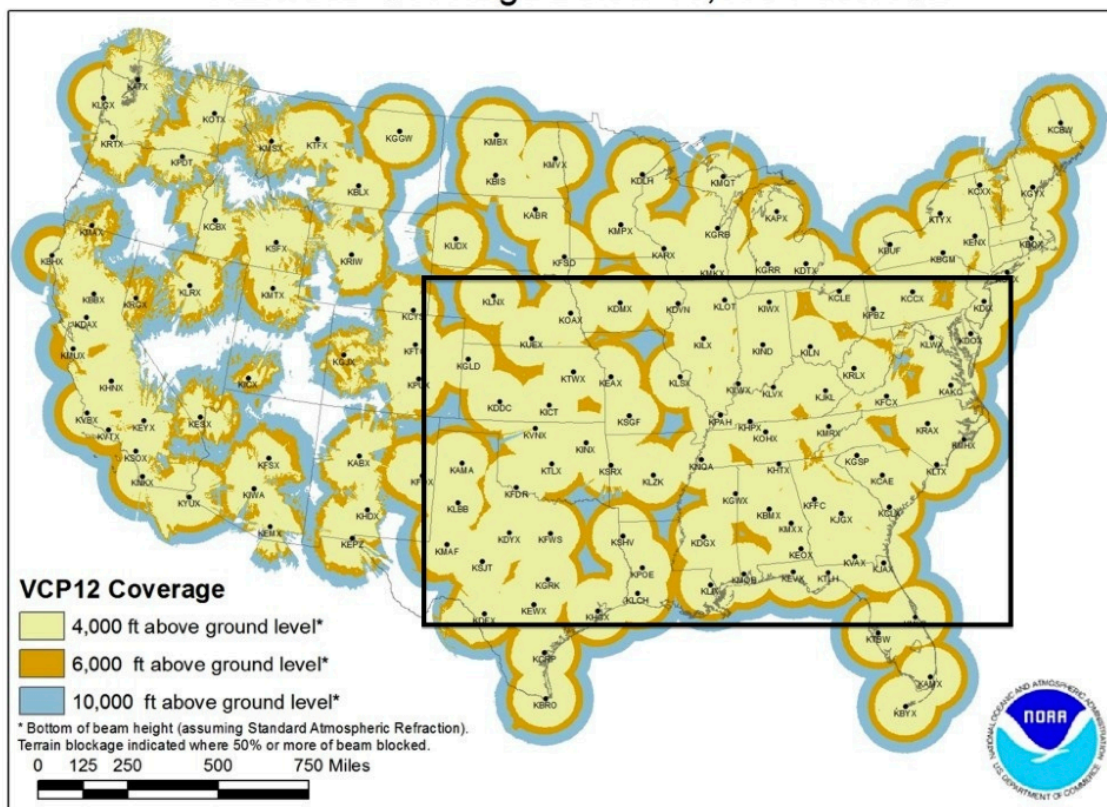## NEXRAD Coverage Below 10,000 Feet AGL

Figure 2.1: Map of NEXRAD radar coverage below 10,000 feet provided by NOAA. Black box designates the geographical area encompassed in this study.

and the current weather conditions around the radar site. When there is convection in the vicinity of the site, the radar operates in 'convective mode'. In convective mode the radar completes a volume scan in approximately 4.5-5 minutes. The typical volume scan time in the absence of convection is $\sim$10 minutes. The maximum detection range of a NEXRAD radar is dependent on the variable being observed. The maximum effective measuring distance is 230 km for radial velocity and 460 km for reflectivity (*Crum and Alberty*, 1993).

2.2   ERA-Interim Reanalysis

Tropopause heights are calculated from atmospheric temperatures and geopotential heights taken from the interim version of the European Center for Medium-Range Weather Forecasts (ECMWF) global atmospheric reanalysis (ERA-Interim). The reanalysis is produced with a sequential data assimilation scheme. For each analysis cycle, observations are combined with information from a forecast model to estimate the evolving state of the atmosphere (*Dee*, 2011). Reanalysis data are available daily at 00, 06, 12, and 18 UTC on a Gaussian grid with a longitude-latitude resolution of $0.75°\times \sim 0.75°$ and 37 unevenly-spaced pressure levels in the vertical. For this study the data have been interpolated horizontally to a $1.5°\times 1.5°$ regular longitude-latitude grid ($\sim$160 km).

2.3   Radiosonde Data

Radiosonde data from stations within the study region are used to evaluate the quality of the tropopause heights calculated from the ERA-Interim analysis. The radiosondes are operated by the National Weather Service (NWS) and are launched from NWS sites around the country. Radiosondes are typically available twice daily at 00 and 12 UTC; additional radiosondes may be launched on an 'as needed' basis if there are severe weather conditions present or expected in the area. The vertical

resolution of each profile is ∼30 meters. For the tropopause height verification 49 radiosonde stations located within the study region are used. Only radiosondes launched at 00 UTC are included, resulting in a total of 13,437 comparison points.

3. METHODS

Tropopause-penetrating convection is identified by the occurrence of NEXRAD echo-tops above the tropopause, as determined from the ERA-Interim analysis. The altitude difference ΔZ is defined as

$$\Delta Z = Z_e - Z_t \tag{3.1}$$

where Z_e is the echo-top height and Z_T is the tropopause altitude. Echo-top height Z_e is calculated from a three-dimensional reflectivity dataset created by combining data from individual radars into a regional composite. Compositing is done using the methods discussed in *Homeyer* (2013). For this analysis, composite reflectivities based on ~100 radar stations are calculated at eight daily synoptic times (00, 03, ..., 21 UTC) using the Level 2 data that fall within $\pm$ 10 minutes of the analysis time. Radar data files are first converted from their native format to netCDF files using the NOAA Weather & Climate toolkit. The volume scans are interpolated from the radar spherical grids to a regular 0.02° (~2 km) longitude-latitude grid, and then linearly interpolated to the 3-hour synoptic analysis times using the two volume scans closest to each analysis time. Vertical reflectivity profiles at each horizontal grid point are created by merging the data from all available radars. This yields a three-dimensional grid with irregularly-spaced observations in the vertical dimension. Once the merging is complete, the three-dimensional irregular composites are interpolated linearly to a regular vertical grid with a resolution of 1 km. If at least 3 radars contribute to sampling a column, the sampling error for that column can be shown to be less than or equal to 1 km; therefore echo top heights are estimated only where at least three

contributing radars sample a column to ensure accuracy. Additionally, as shown by *Homeyer* (2013), the sensitivity of radar detection decreases as range from the radar increases. The maximum distance from the radar used for compositing is 300 km. At this distance the minimum detectable radar return signal is 7.5 dB, so a reflectivity threshold of 10 dB is used to determine the echo top height for each column.

ERA-Interim data are interpolated in space and, if necessary, in time in order to calculate tropopause heights at the temporal and spatial resolution of the composite radar files. For hours that fall on the ERA-Interim analysis times (00, 06, 12, and 18 UTC), the tropopause height is computed by first interpolating temperature and geopotential height horizontally in space to a $0.02° \times 0.02°$ grid, which matches the composite radar grid. Each temperature column is then interpolated to a vertical resolution of 100 meters using cubic splines. The World Meteorological Organization (WMO) definition (*WMO*, 1957) is applied to determine primary and secondary tropopause locations as outlined in *Homeyer et al.* (2010). To calculate tropopause height for the intermediate times (03, 09, 15 and 21 UTC), temperature and geopotential height are first interpolated linearly in time to the desired analysis time before following the above procedure. The altitude difference ΔZ is then computed using equation 3.1. The final analysis product is 3-hourly maps of ΔZ for all of 2004.

4.   RESULTS

4.1   Tropopause Calculation Validation

To evaluate the accuracy of tropopause heights estimated from the ERA-Interim reanalysis, the ERA-Interim tropopause is compared to tropopause heights calculated from high-resolution radiosonde profiles. Radiosonde tropopause heights are calculated following the WMO definition described in section 3. The high-resolution ERA-Interim tropopause height is interpolated to the location of the sonde launch site and the heights from the two different sources are compared. Figure 4.1 shows that ~77% of heights are within ± 0.5 km of each other, and ~91% of points are within ±1 km of each other. The vertical resolution of the model in the area of the tropopause is ~1 km.

There are two distinct populations of points present in Figure 4.1. The first (and largest) contains points that fall close to the the 1-to-1 line; the second contains points with ERA-Interim tropopause heights that are significantly higher than the radiosonde calculated values (ellipse in Figure 4.1). The occurrence of this second population of points has been previously documented when comparing model-calculated tropopause heights to radiosonde observations. Figure 4 of *Homeyer et al.* (2010) compares Global Forecast System (GFS) tropopause heights to radiosonde data and shows a distribution of points very similar to what is observed in this analysis. *Homeyer et al.* (2010) determined the presence of these points is primarily due to the lower vertical resolution of the model. Because of this lower resolution the simulated fields are unable to accurately represent the complicated atmospheric structure present near the sub-tropical jet. In these situations, when the WMO tropopause detection algorithm is applied to the model field, the primary tropopause is not
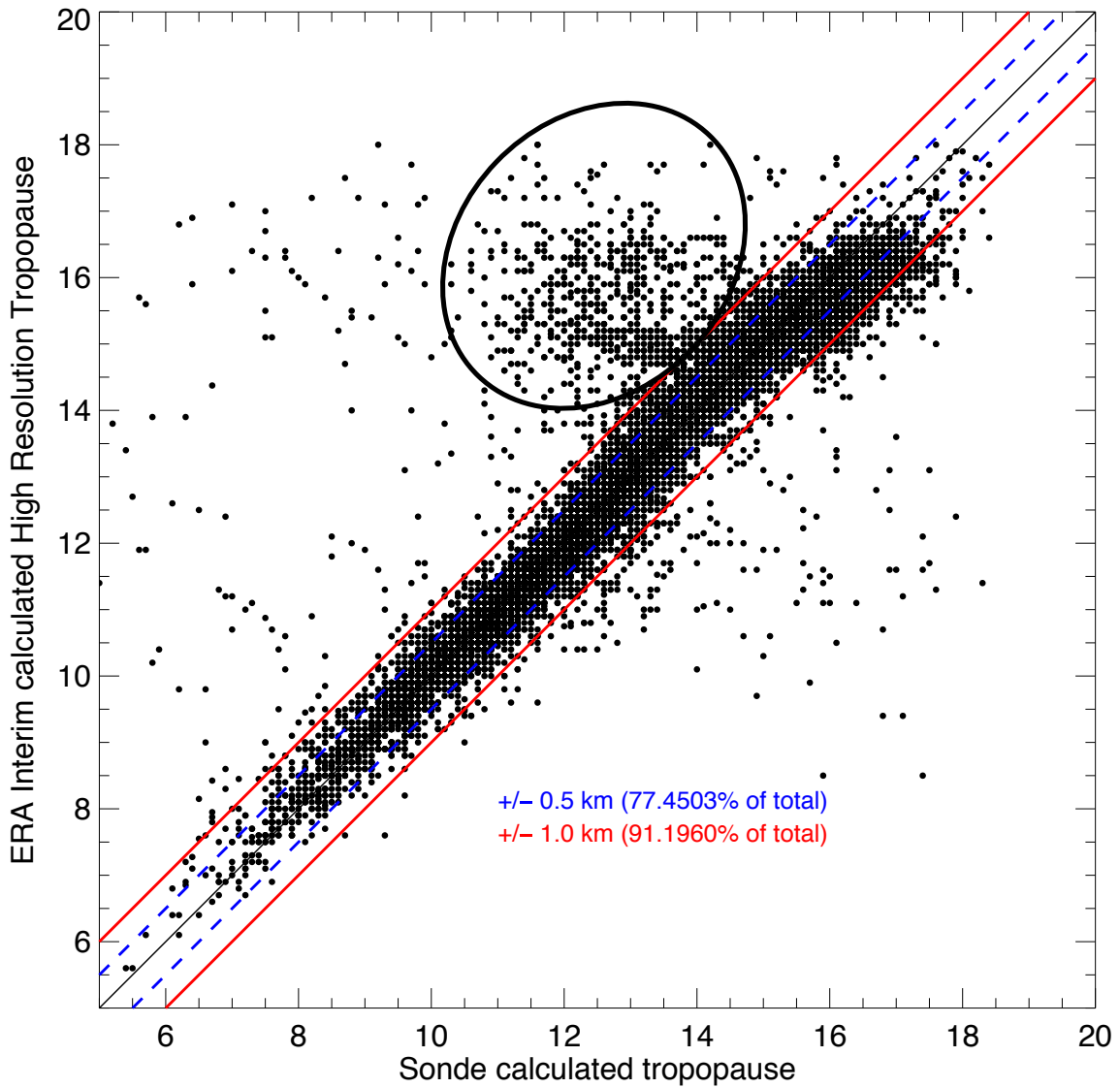
11

Figure 4.1: Comparison of ERA-Interim high-resolution calculated tropopause height to NOAA balloon sonde tropopause height. Red lines denote a ±1 km boundary around perfect agreement, blue lines are ±0.5 km. The ellipse is explained in text.

identified, and the secondary tropopause is erroneously identified as the primary tropopause. Because the vertical resolution of the radiosonde data is much higher, incorrect tropopause identification using sonde data is much less likely. When the circled population of points are removed ∼81% of points are within ± 0.5 km and ∼96% of points are within ±1 km of each other. An additional source of error in Figure 4.1 stems from interpolating ERA-Interim tropopause heights to the time and location of the sonde launch, not to the time or location where the sonde actually crossed the tropopause.

Although the circled population of points in Figure 4.1 does not make up a large portion of the total population (∼6%), they are of interest for this analysis. A recent modeling study by *Homeyer et al.* (2013) showed that some of the deepest penetrating convective storms occur in an environment where a double tropopause is present. The magnitude of overshooting convection events that occur in locations where the WMO algorithm incorrectly identifies the secondary tropopause as the primary tropopause will be underestimated. This may result in convective events that penetrate the tropopause by several kilometers being classified as much shallower in the analysis, or these events could be missed entirely. These tropopause misidentifications occur throughout the study area, but are most prevalent in the southern portion of the domain.

4.2   Radar Coverage

Figure 2.1 shows the NEXRAD network coverage for the contiguous U.S. Because the radar data coverage is irregular in both space and time, we first assess how well the composited NEXRAD observations sample the study area. Figure 4.2 shows the percentage time each location in the study area is sampled by at least 3 radars. The actual radar coverage over the study domain shown in Figure 4.2 differs from what

is shown in Figure 2.1 for several reasons: 1) a contribution of at least three radars in a column is required for the echo-top estimate, 2) data from several stations are unavailable for the entire year, and 3) data availability changes throughout the year due to radar operating status and data archiving issues. Individual station locations are plotted in Figure 4.2 and color coded based on their data availability. Stations in orange have no data available throughout the entire study period, stations in white have data available for at least part of the study period. Coverage is best across the central part of the study area, with a few exceptions. There are several radars in the southeast and Texas for which no data are available during the entire study period, resulting in relatively poor coverage across this area. Coverage across the northern boundary of the region is also lacking for the same reason. In the remainder of this paper, the occurrence of tropopause-penetrating convection is expressed as a percentage of the maximum possible area covered by three or more radars, which we designate as A_{max}. A_{max} is the area covered by colors in Figure 4.2, excluding the area shown in gray, for which no data are available during the year. A_{max} is XX% of the total area of the map in Figure 4.2

Data availability also changes with time due to operational and data archiving issues. Changes in radar operating status are quite common and occur irregularly throughout the study period. No stations operated continuously throughout the study. Because many locations are observed by more than three radars, however, the loss of a single radar does not necessarily mean that a tropopause-penetrating convective event will go undetected. As seen in Figure 4.2 the relatively dense distribution of radar sites throughout the study domain ensures that many locations are sampled by more than the three radars we require for inclusion. Approximately 65% of the study area is sampled by four or more radars throughout the study period. This means that across much of the study area, the loss of any single radar does not

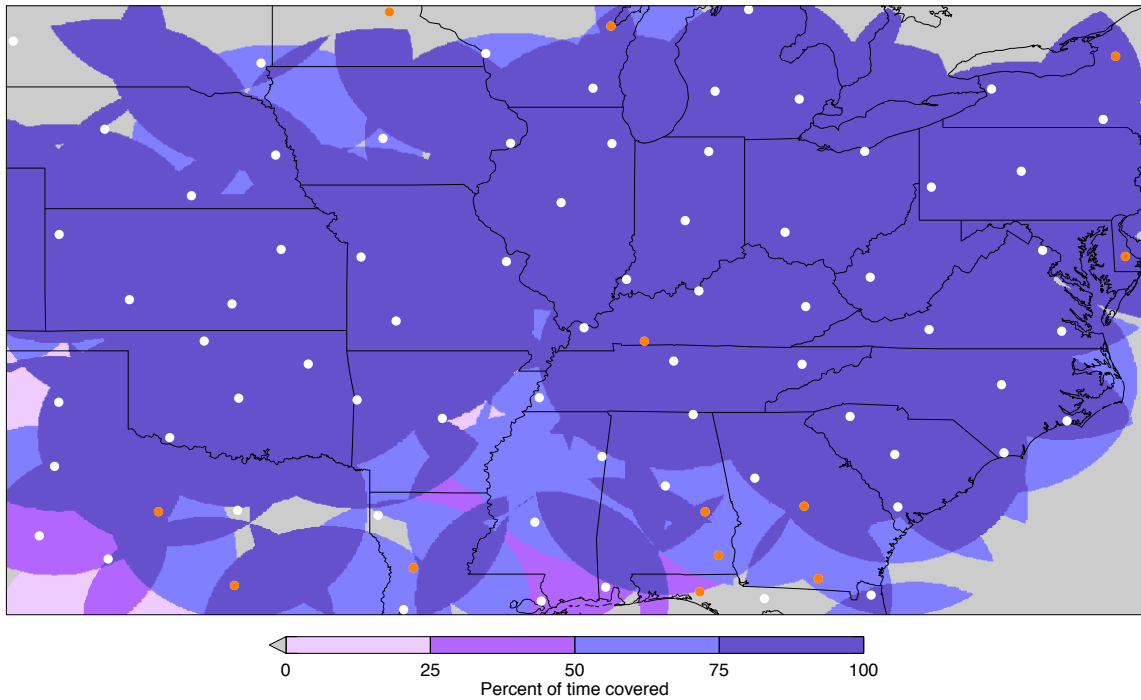Figure 4.2: Map showing the percent time each point in the study domain has at least three radars sampling its column. Gray color indicates the column is never sampled with at least three radars. Colored points indicate radar locations and data availability. White denotes a station with data available during the study period, orange denotes a station with no data available throughout the study time.

necessarily compromise the detection ability of the system as a whole.

Figure 4.3 shows data availability for 2004 as a percentage of A_{max}. The white area indicates the fraction of A_{max} covered by four or more radars; gray is the fraction covered by three radars; and black is the fraction covered by two or fewer radars. Figure 4.3 shows that coverage remains at $\sim$90% for throughout the year, with fluctuations as individual radar sites come on and off line and occasional short gaps for the entire network. The uptick in coverage starting in the middle of March occurs because several radars in the southern portion of the study area which had no data available up until that time return to operational status.

Coverage by three or more radars as a function time of day is also examined. As with Figure 4.3 this coverage is expressed as a percentage of A_{max}. Percent coverage at each three-hourly analysis time is nearly constant, with coverage percents ranging between 82% at 00 UTC and 89% at 03 and 21 UTC, with no obvious systematic bias present. The lack of annual and diurnal sampling biases in NEXRAD coverage area leads leads us to conclude that any observed diurnal or annual cycles of overshooting convection are genuine, and not an artifact of coverage issues.

Requiring at least three radars to sample a column will also decrease the coverage area of the radar network. Figure 4.4 shows a year long time series of cumulative percent area over the entire study domain. This percent area measure how much of the study area is covered by convection that reaches the level of the tropopause or higher with a one, two, and three radar sampling requirement. As evidenced in this figure, the percent area of the study domain covered by detections is $\sim$8% higher when using a one radar requirement vs. requiring three radars to sample a column. It is important to note that the largest events (labeled A in Figure 4.4) are detected no matter what the radar requirement is. The main differences in detection area occur over many smaller events that are not detected by using the higher radar
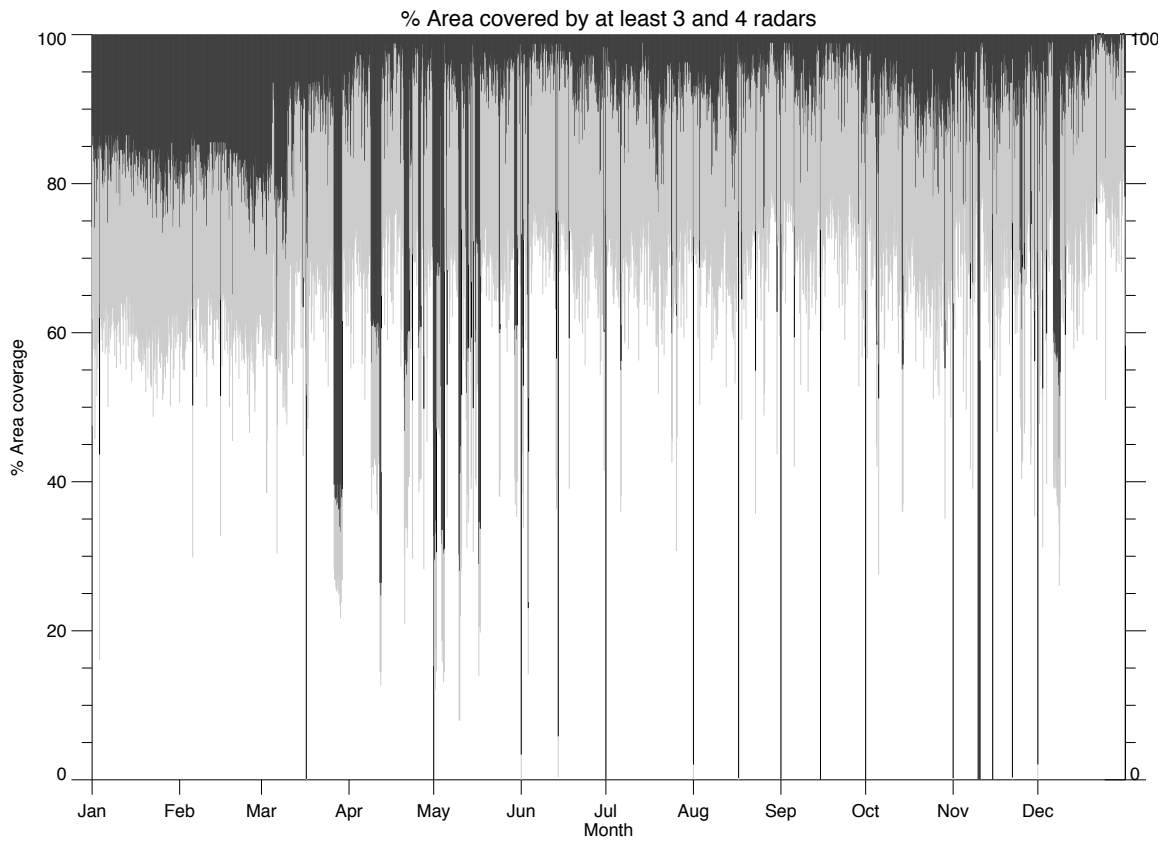
Figure 4.3: Time series showing percent of study area covered by two or fewer radars (black), by three radars (gray), and by four or more radars (white) as a function of time. Points within the study domain that are never sampled by three or more radars are excluded from this calculation.
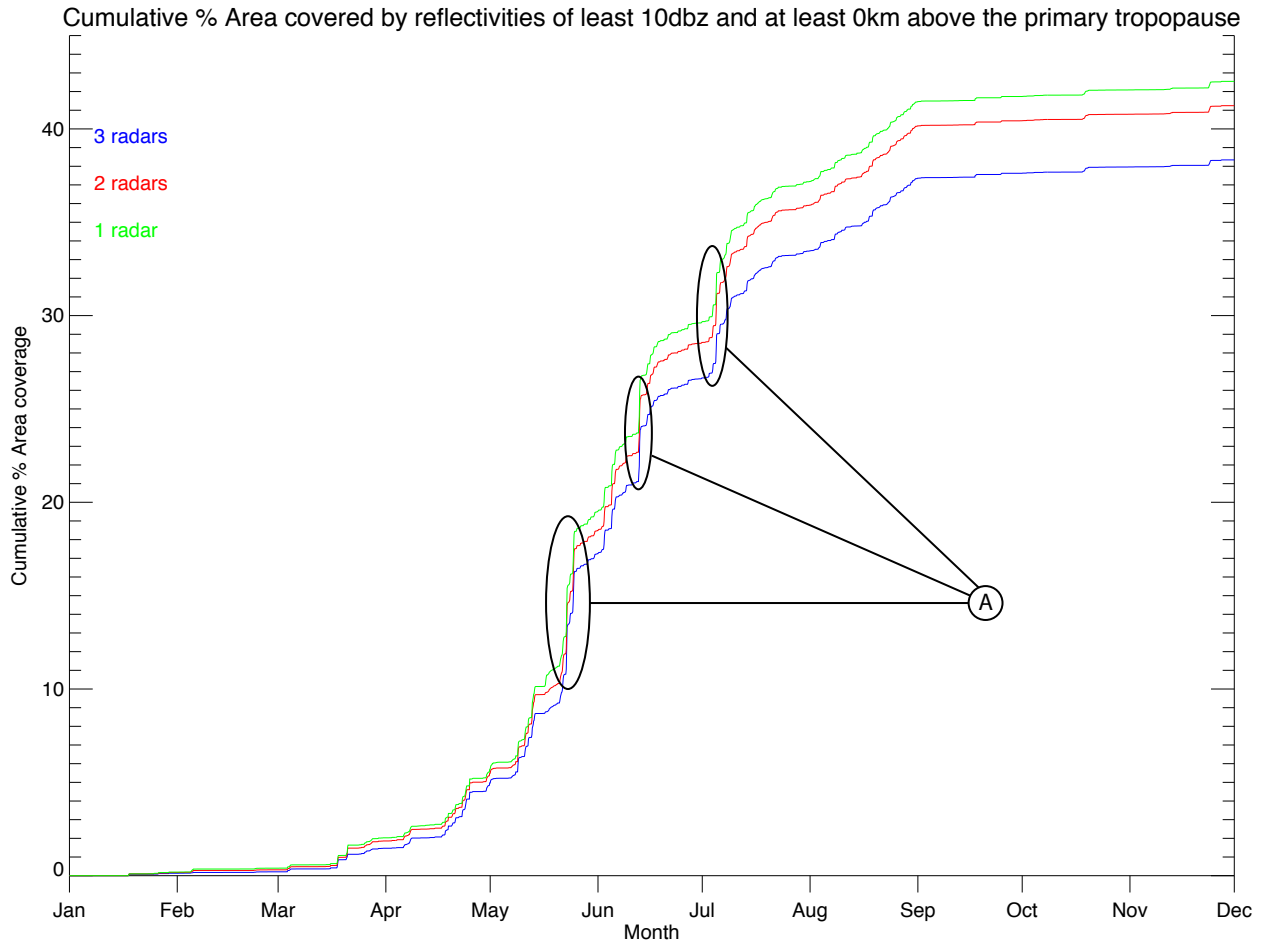
17

Figure 4.4: Cumulative percent area coverage of convection reaching at least the level of the tropopause using a one, two, and three radar sampling requirement for each column. Marked areas are discussed in text.

requirement. It is also very important to note that simply because the one radar requirement detects a larger area amount of deep convection does not mean it is more correct. As discussed in section 3 a minimum of three radars was required to keep the vertical sampling error less than 1 km. Using a smaller radar requirement results in more overshooting identifications, but will also lead to a larger number of false positives.

4.3 Analysis

Figure 4.5 is an example of instantaneous maps of composite radar reflectivity (top) and ΔZ (bottom) for a single time step in June 2004. On this day there are several deep convective systems present within the study area, some penetrating 4-5 km above the tropopause. Figure 4.6 is a vertical cross section through the deep convection occurring near the Kansas-Nebraska border (line segment labeled AB in Figure 4.5). Colors indicate reflectivity; black lines denote the primary and secondary tropopauses. In this example convection has penetrated $\sim$5 Km above the primary tropopause, and, in some locations, $\sim$1 Km above the secondary tropopause. Although the focus of this study is on the statistical characteristics of overshooting convection, it is worth noting that the high vertical resolution of the composite product allows detailed observation of individual storms. This compositing method is therefore a useful tool for studying storm structure and related smaller-scale phenomena.

Figure 4.7 shows the annual cumulative occurrence of radar reflectivities of at least 10 dBZ that reach the level of the primary tropopause or higher as a function of time of day, expressed as a percentage of A_{max}. A strong diurnal cycle is present, with the highest likelihood of tropopause-penetrating events occurring around 00 UTC (7:00 PM Central Daylight Time (CDT)) and the lowest likelihood occurring around 12-18 UTC (7:00 AM - 1:00 PM CDT).

Figure 4.8 shows the cumulative occurrence of convection reaching the tropopause as a function of month. A strong annual cycle can be seen, with a distinct peak in the late spring and early summer months. These results are consistent with the annual cycles of the occurrence of deep convection and of tropopause height. Northern hemisphere mid-latitude tropopause heights are lowest in the winter months, with

19

Composite Radar Reflectivity
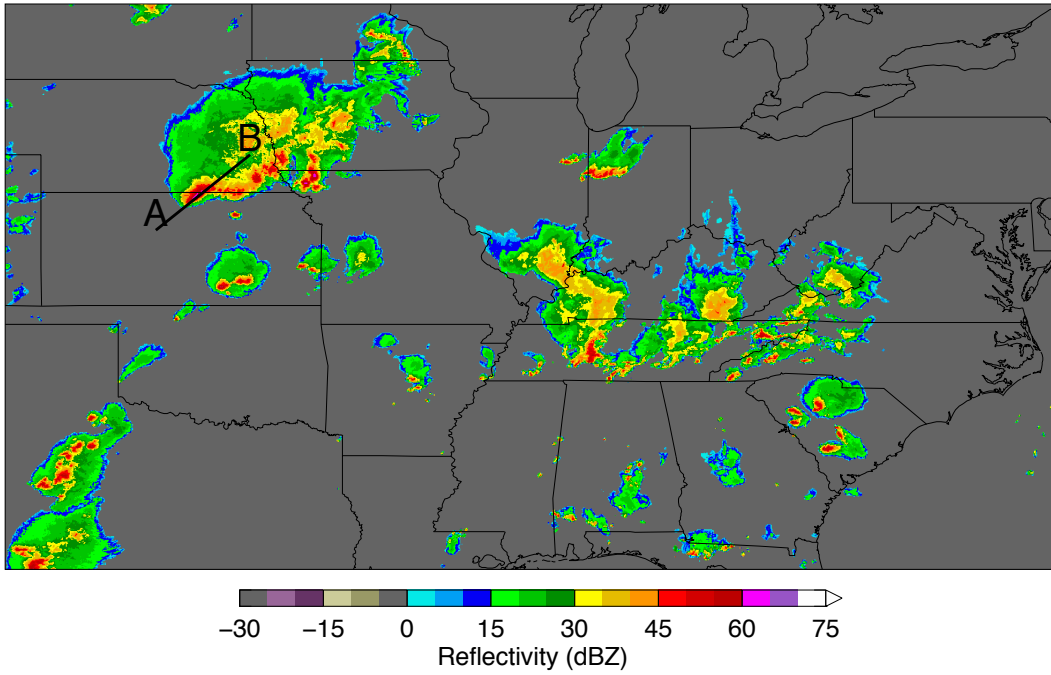
Echo-Top Height Relative to the Tropopause
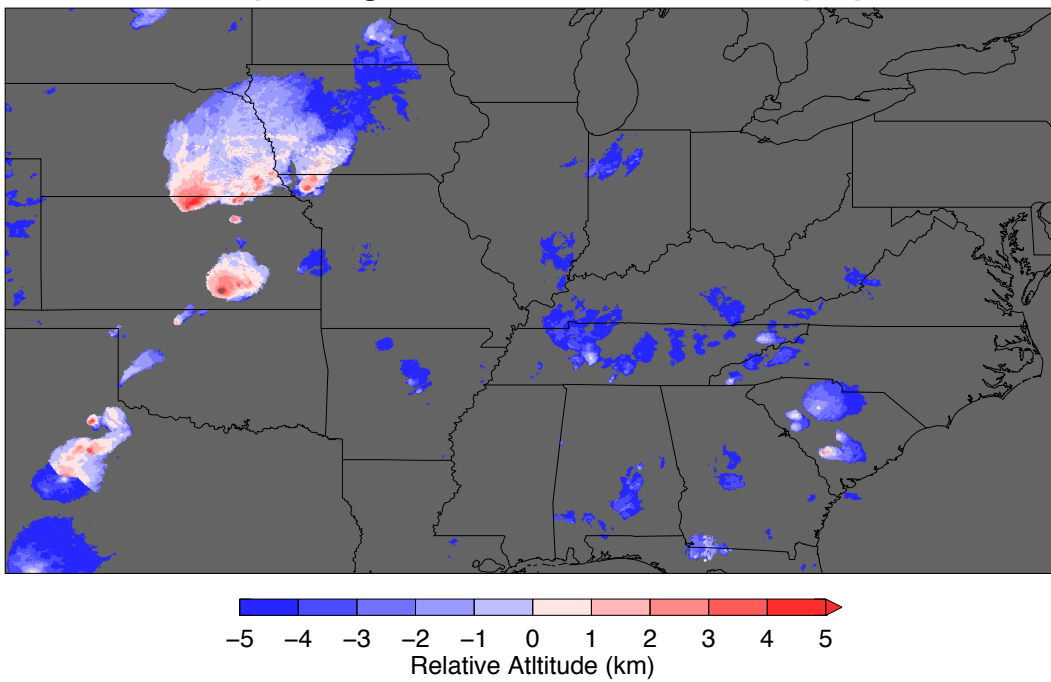
Figure 4.5: Composite radar reflectivity in dBZ (left) and echo-top height relative to the tropopause ΔZ in km (right) for 2004-06-13 00Z. Line A-B in the top panel marks the location of the cross section in Figure 4.6

Figure 4.6: Radar reflectivity cross section along the line A-B shown in Figure 4.5. Black lines are the ERA-Interim primary and secondary tropopause.

Figure 4.7: Cumulative percentage coverage over the year at each 3-hourly analysis time relative to A_{max}.
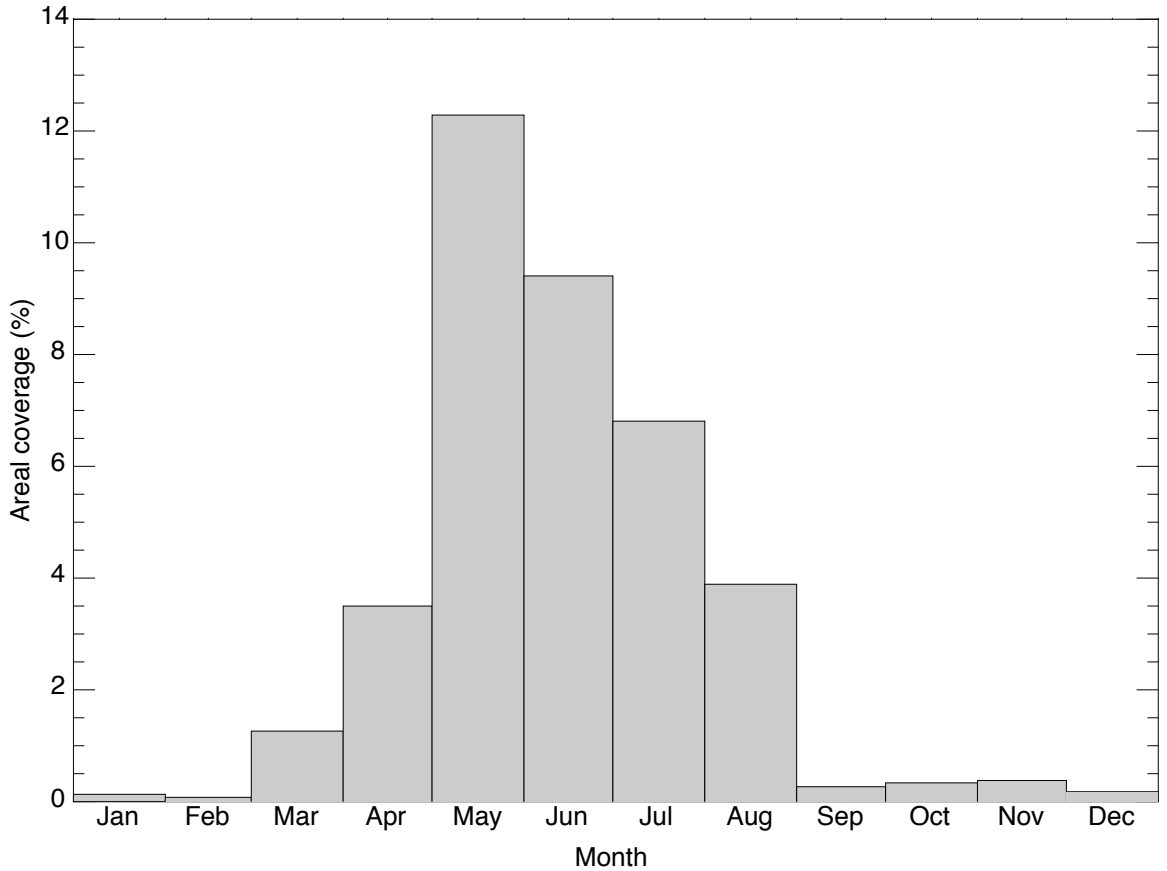
Figure 4.8: Cumulative percentage coverage within each month relative to A_{max}.

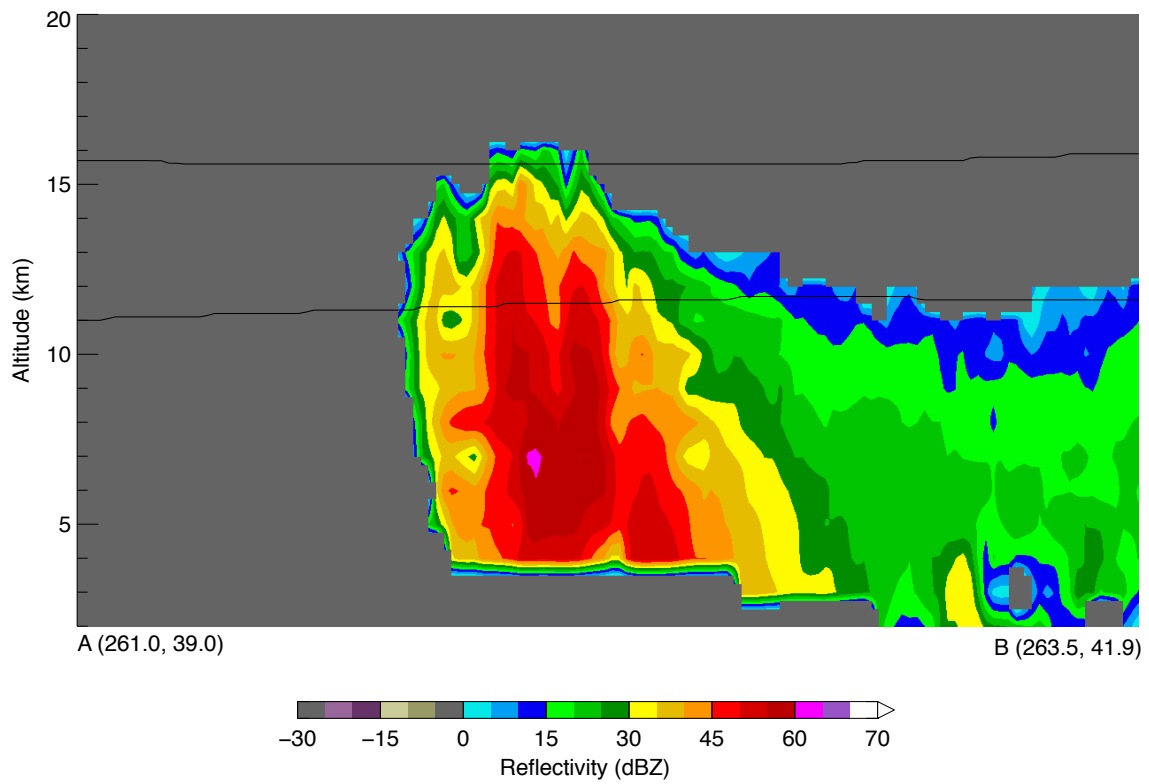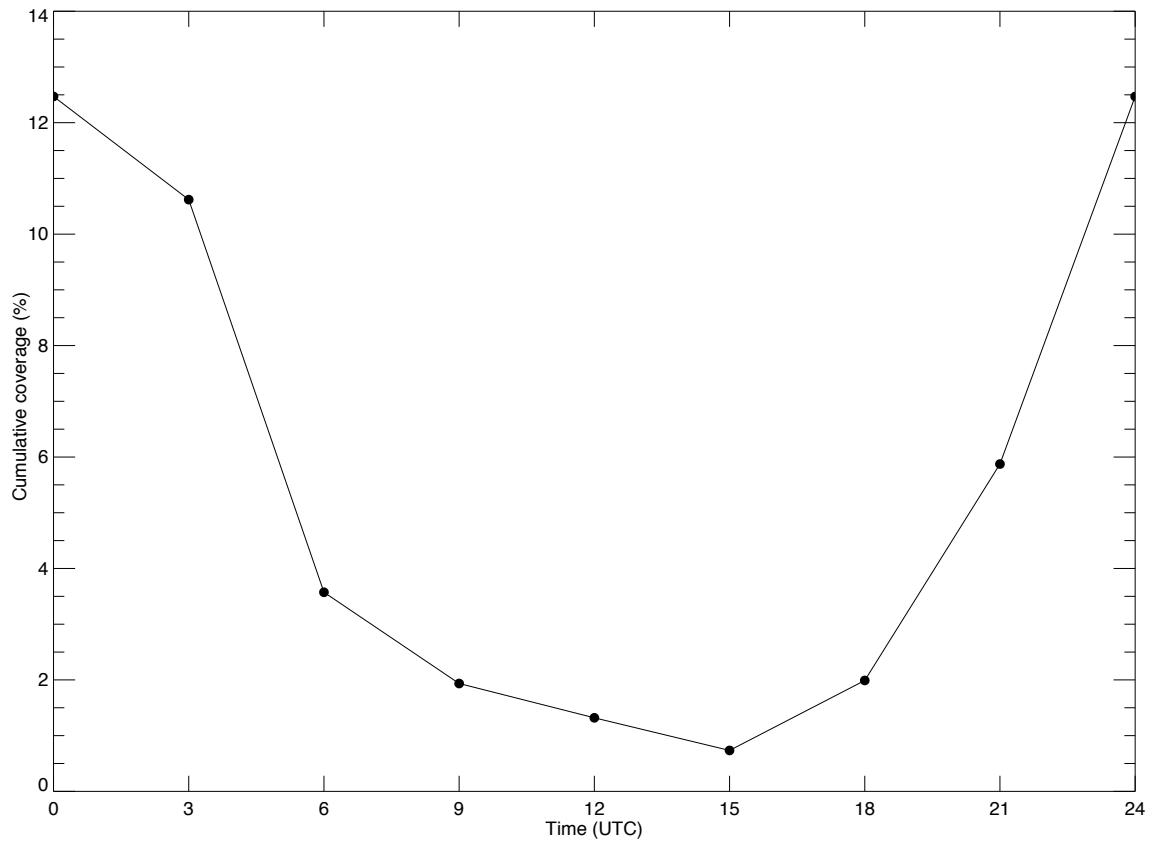average height increasing through the summer before decreasing again starting in the fall (*Wong and Wang*, 2000). Also around this time the amount of convection occurring is also increasing. The combination of these two cycles results in late spring and early summer having the largest occurrence of tropopause-penetrating convection events.

Figure 4.9 shows the occurrence of echo-tops above the tropopause for each 3-hour analysis time throughout the year. The blue line is the cumulative total of overshooting from the beginning of the year. Although the largest amount of total overshooting occurs in May of this year, Figure 4.9 shows that the largest single

event occurs in June, and that much of each month's total occurs as the result of several large individual events. This raises the question of how much influence a three-hour time step has on the total amount of overshooting convection detected. Because the majority of each months contribution comes from several large events, and the lifetimes of these events above the tropopause can be relatively short, it is possible that a time step of three hours results in several of these large events being missed entirely. As an example of how large an effect this might have, decreasing the temporal resolution from 3 to 6 hours results in the cumulative percent area covered by overshooting convection decreasing by a factor of two.

The geographical pattern of total occurrence over the year is shown in Figure 4.10. This map counts the number of times during 2004 that each location experiences a reflectivity of 10 dbz that reaches the level of the tropopause or higher. Figure 4.10 shows overshooting convection events are most common over the high plains, particularly in Nebraska and Kansas and very few occurrences east of the Mississippi river. There are very few occurrences of overshooting convection detected in the southeast portion of the United States. The 5-year climatology created infrared window brightness temperatures and modeled tropopause temperatures by *Bedka et al.* (2010) found a distinct maxima of overshooting convection in the southeast region. The reason for the discrepancy between these methods is not fully understood. *Bedka et al.* (2010) also performed a climatology of pixels colder than the tropopause but not classified as overshooting by their algorithm. The distribution of these points very closely matches the distribution of occurrences seen in 4.10. Future studies spanning a longer time period will help assess whether the absence of overshooting convection events in the southeast is a single-year anomaly for 2004 or a persistent trend.

Figure 4.11 is an estimate of the volume of air reaching different altitudes above
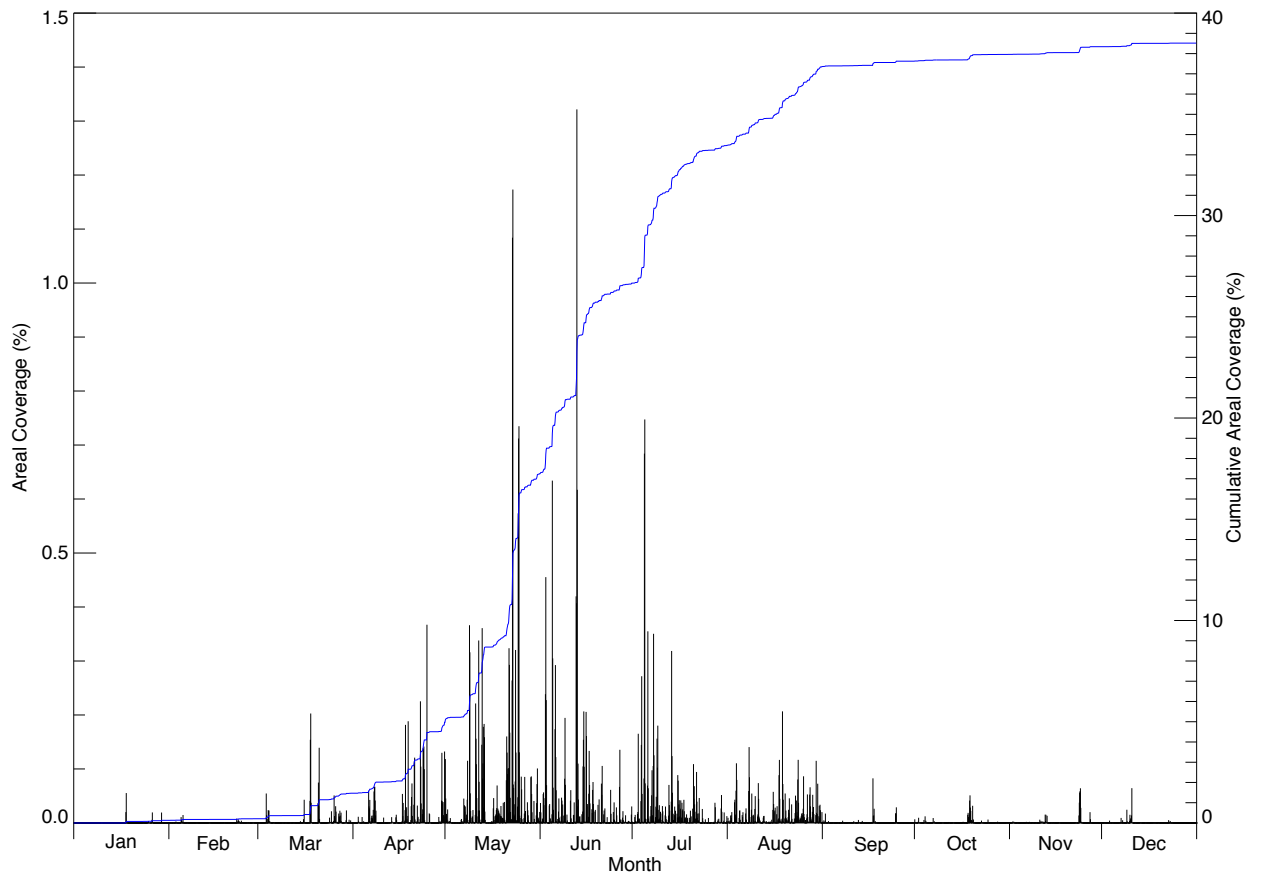
24

Figure 4.9: Year long time series. Black lines represent percent area of the sampled study domain covered by convection reaching at least the level of the tropopause at each time step. The blue line is a running cumulative total percent area of the sampled study area covered by that convection.

25
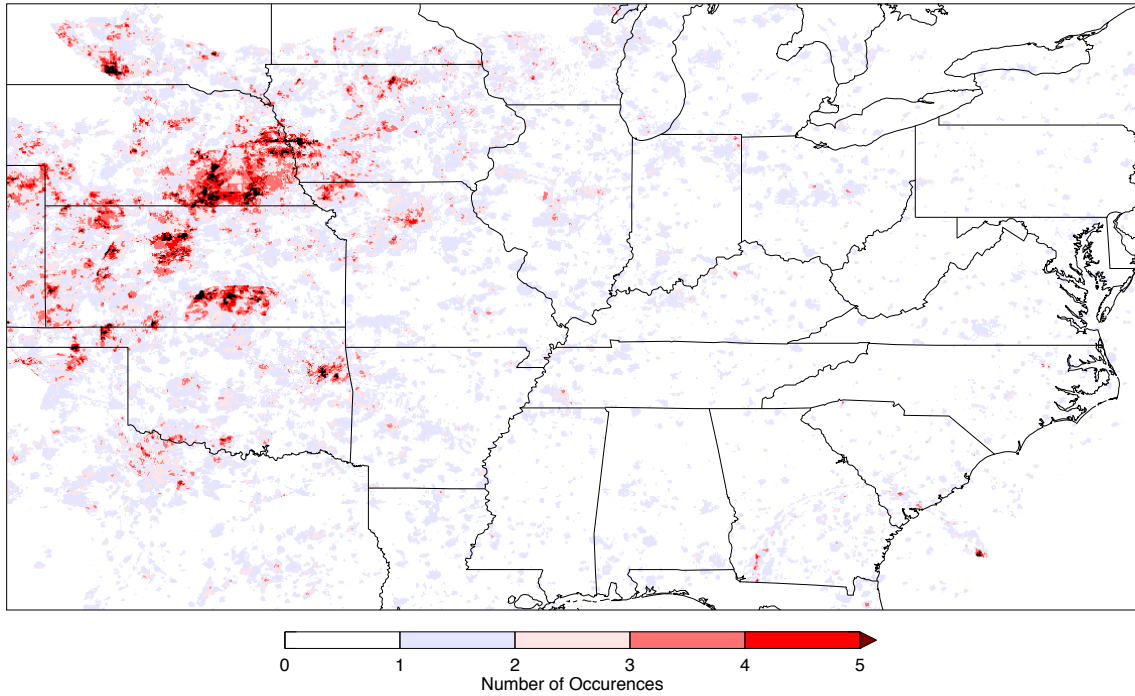
Figure 4.10: Map showing number of occurrences over the year 2004 where reflectivities of at least 10 dBz reach at least the altitude of the tropopause.

the tropopause. This is computed by taking the storm top relative altitude (ΔZ) and multiplying it by the associated column area. The total volume of overshooting decreases rapidly as a function of height above the primary tropopause. It is important to note that, as with the cumulative percent area plot (Figure 4.9), the total volume of overshooting is also dependent on the temporal resolution of the data. Choosing a smaller time step would result in a larger total overshooting volume, down to a limit where the results don't change between time steps, though the relationships between the different ΔZ levels should remain the same.

Figure 4.11: Total volume of overshooting for the entire year of 2004 binned by altitude relative to the ERA-Interim tropopause.

5. SUMMARY

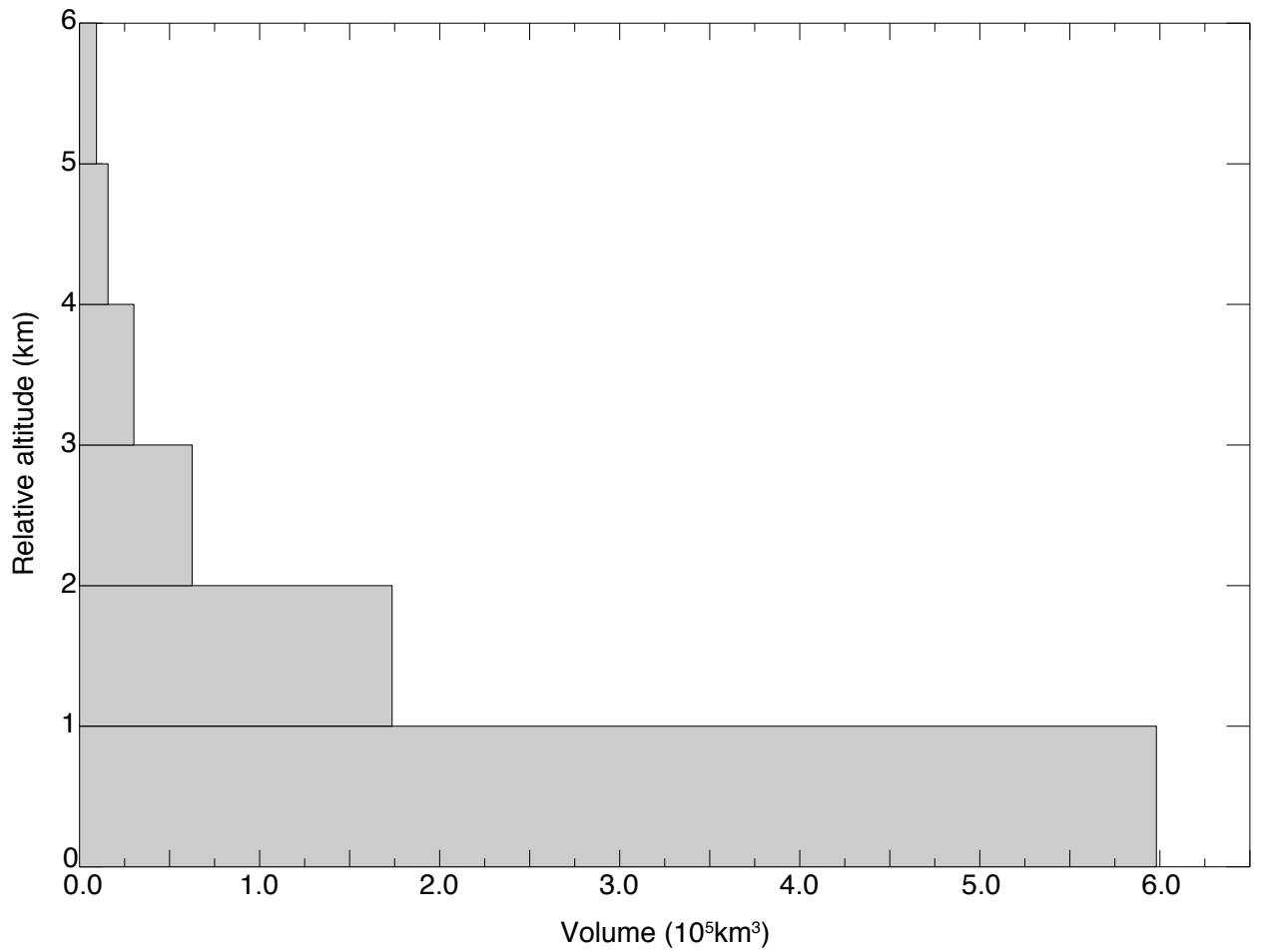This study uses a new method of compositing individual NEXRAD WSR-88D stations into a regional grid with high horizontal and vertical resolution in order to diagnose the frequency, magnitude, and location of tropopause-penetrating convection events. Tropopause altitudes estimated from the ERA-Interim Reanalysis show good agreement with high-resolution NOAA radiosonde data. In about 5% of cases within the study area, the ERA-Interim data fail to represent the primary tropopause, probably due to limited vertical resolution. This results in the secondary tropopause being incorrectly identified as the primary tropopause, with a consequence that some storms that penetrate the tropopause may not be identified as such.

For 2004 the NEXRAD network provides a high level of areal coverage, with at least three or more radars available throughout most of the study area. Despite frequent fluctuations of radar coverage during the study period, there are no obvious annual or diurnal sampling biases present that would affect the diurnal or annual statistics. There are several areas within the study domain that likely suffer from undersampling due to the lack of operational NEXRAD sites in their vicinity for the entire study period. These areas include the Northern boundary of the study domain, and the southeast corner of the United States. Because of this undersampling, detection within these areas may be limited or nonexistent during certain time periods.

Analysis of a single date shows that the compositing method works well and generates accurate regional reflectivity fields. A cross section through a single deep convection event revealed reflectivities of 10 dBZ penetrating $\sim$5 km above the tropopause

and, in some locations, reaching 1 km above the secondary tropopause. Events of this magnitude are relatively rare during the study period, though because of their relatively short lifetime, a higher temporal resolution would likely increase the number of large events detected by the network.

A strong diurnal cycle is present with a peak around 00 UTC and a minimum at 15 UTC. This peak is consistent with previous analyses of the diurnal cycle of convection over the U.S. There is also a distinct annual cycle present in both the overall monthly percent area of the study domain covered by overshooting convection, and in the magnitude of individual events that contribute to the monthly total. The area of overshooting reaches a peak during May and is small from September to February. The largest individual event occurred in June. Single, large, events make up a significant portion of each month's total percent area of overshooting. As stated before, higher temporal resolution would likely detect more of these large events, and lead to an increase in the cumulative area of overshooting convection.

Occurrence maps show that tropopause-penetrating convection is most common over the high plains, and least common east of the Mississippi. The lack of occurrences in the southeast differs from the findings of a five year climatology performed by *Bedka et al.* (2010). The same study also identified a large number of points colder than the tropopause which were not classified as overshooting by their algorithm but whose distribution of occurrence closely matches ours.

An assessment of the total volume of overshooting convection as a function of relative altitude shows that many of the overshooting storms reach less than 1 km above the tropopause, and the amount of overshooting volume falls off rapidly with increasing relative altitude.

Overall, compositing individual radars into a single regional grid appears to provide a high-quality three-dimensional field of radar reflectivity. The coverage over

the study domain is generally good, and suffers only in areas where NEXRAD sites are non-operational for long periods of time. Further work is planned to extend the analysis to a longer time period and to higher temporal resolution in order to assess the inter-annual variability of overshooting convection events and construct a long-term climatology. Other studies using this NEXRAD compositing method are also underway using the dual-polarization upgrade to the NEXRAD network in order to examine storm structure in detail.

REFERENCES

Ackerman, S. A. (1996), Global satellite observations of negative brightness temperature differences between 11 and 6.7 μm, *J. Atmos. Sci.*, *53*, 2803–2812.

Adler, R. F., M. J. Markus, and D. D. Fen (1983), Thunderstorm top structure observed by aircraft overflights with an infrared radiometer, *J. Climate Appl. Meteor.*, *22*, 579–593.

Alcala, C. M., and A. E. Dessler (2002), Observations of deep convection in the tropics using the Tropical Rainfall Measuring Mission (TRMM) precipitation radar, *J. Geophys. Res.*, *107*(D24), 4792, doi:10.1029/2002JD002457.

Anderson, J. G., D. M. Wilmouth, J. B. Smith, and D. S. SayresS (2012), UV dosage levels in summer: Increased risk of ozone loss from convectively injected water vapor, *Science*, *337*(6096), 835–839.

Bedka, K., J. Brunner, R. Dworak, W. Feltz, J. Otkin, and T. Greenwald (2010), Objective satellite-based detection of overshooting tops using infrared window channel brightness temperature gradients, *J. Appl. Meteor. Climatol.*, *49*, 181–202, doi:10.1175/2009JAMC2286.1.

Berendes, T. A., J. R. Mecikalski, W. M. M. Jr., K. M. Bedka, and U. S. Nair (2008), Convective cloud identification and classification in daytime satellite imagery using standard deviation limited adaptive clustering, *J. Geophys. Res.*, *113*(D20), 207, doi:10.1029/2008JD010287.

Changon, J. M., and S. L. Gray (2010), A comparison of stratosphere-troposphere transport in convection-permitting and convection-parameterizing simulations

of three mesoscale convective systems, *J. Geophys. Res.*, *115*(D24), 318, doi: 10.1029/2010JD014421.

Crum, T. D., and R. L. Alberty (1993), The WSR-88D and the WSR-88D operational support facility, *Bull. Amer. Meteor. Soc.*, *74*(9), 1669–1687.

Dai, A., F. Giorgi, and K. E. Trenberth (1999), Observed and model-simulated diurnal cycles of precipitation over the contiguous United States, *J. Geophys. Res.*, *104*(D6), 6577–6402.

Dee, D. P. (2011), The ERA-Interim reanalysis: configuration and performance of the data assimilation system, *Q. J. R. Meteorol. Soc.*, *137*, 533–597, doi: 10.1002/qj.828.

Dessler, A. E. (2002), The effect of deep, tropical convection on the tropical tropopause layer, *J. Geophys. Res.*, *107*(D3), 4033, doi:10.1029/ 10.1029/2001JD000511.

Fischer, H., M. de Reus, M. Traub, J. Williams, J. Lelieveld, J. de Gouw, C. Warneke, H. Schlager, A. Minikin, R. Scheele, and P. Siegmund (2003), Deep convective injection of boundary layer air into the lowermost stratosphere at midlatitudes, *Atmos. Chem. Phys.*, pp. 739–745.

Forster, P., and Co-authors (2007), *Climate Change 2007: The Physical Science Basis*, chap. 2. Changes in Atmospheric Constituents and in Radiative Forcing, pp. 129–234, Cambridge University Press, Cambridge, UK.

Fritz, S., and I. Laszlo (1993), Detection of water vapor in the stratosphere over very high clouds in the tropics, *J. Geophys. Res.*, *98*(D12), 22,959–22,967.

Fromm, M. D., and R. Servranckx (2003), Transport of forest fire smoke above the tropopause by supercell convection, *Geophys. Res. Lett.*, *30*(10), 1542, doi: 10.1029/2002GL016820.

Gettelman, A., M. L. Salby, and F. Sassi (2002), Distribution and influence of convection in the tropical tropopause region, *J. Geophys. Res.*, *107*(D10), 4080, doi: 10.1029/2001JD001048.

Gettelman, A., P. Hoor, L. L. Pan, W. J. Randel, M. I. Hegglin, and T. Birner (2011), The extratropical upper troposphere and lower stratosphere, *Rev. Geophys.*, *49*, doi:10.1029/2011RG000355.

Gray, S. L. (2003), A case study of stratosphere to troposphere transport: The role of convective transport and the sensitivity to model resolution, *J. Geophys. Res.*, *108*(D18), 4590, doi:10.1029/2002JD003317.

Hanisco, T. F., E. J. Moyer, E. M. Weinstock, J. M. S. Clair, D. S. Sayres, J. B. Smith, R. Lockwood, J. G. Anderson, A. E. Dessler, F. N. Keutsch, J. R. Spackman, W. G. Read, and T. P. Bui (2007), Observations of deep convective influence on stratospheric water vapor and its isotropic composition, *Geophys. Res. Lett.*, *34*(L04), 814, doi:10.1029/2006GL027899.

Hegglin, M. I., D. Brunner, H. Wernli, C. Schwierz, O. Martius, P. Hoor, H. Fischer, U. Parchatka, N. Spelten, C. Schiller, M. Krebsbach, U. Weers, J. Staehelin, and T. Peter (2004), Tracing troposphere-to-stratosphere transport above a mid-latitude deep convective system, *Atmos. Chem. Phys.*, *4*(3), 741–756, doi: 10.5194/acp-4-741-2004.

Holton, J. R., P. H. Haynes, M. E. McIntyre, A. R. Douglass, R. B. Rood, and L. Pfis-

ter (1995), Stratosphere-troposphere exchange, *Rev. Geophys.*, *33, 4* (95RG02097), 403–439.

Homeyer, C. R. (2013), Formation of the Enhanced-V infrared cloud top feature from high-resolution three-dimensional radar observations, *J. Atmos. Sci.*, *in press*, doi: 10.1175/JAS-D-13-079.1.

Homeyer, C. R., K. P. Bowman, and L. L. Pan (2010), Extratropical tropopause transition layer characteristics from high-resolution sounding data, *J. Geophys. Res.*, *115* (D13108), doi:10.1029/2009JD013664.

Homeyer, C. R., L. L. Pan, and M. C. Barth (2013), Transport from convective over-shooting of the extratropical tropopause and the role of large-scale lower strato-spheric stability, *J. Geophys. Res.*, *submitted.*

Le, T. V., and W. A. Gallus (2012), Effect of an extratropical mesoscale convective system on water vapor transport in the upper troposphere/lower stratosphere: A modeling study, *J. Geophys. Res.*, *117* (D03), 111, doi:10.1029/2011JD016685.

Leone, D. A., R. M. Endlich, J. Petričeks, R. T. H. Collis, and J. R. Perter (1989), Meteorological considerations used in planning the NEXRAD network, *Bull. Amer. Meteor. Soc.*, *70* (1), 4–13.

Lindsey, D. T., and L. Grasso (2008), An effective radius retrieval for thick ice clouds using GOES, *J. Appl. Meteor. Climatol.*, *47*, 1222–1231.

Martin, D. W., R. A. Kohrs, F. R. Mosher, C. M. Medaglia, and C. Adamo (2008), Over-ocean validation of the Global Convective Diagnostic, *J. Appl. Meteor. Cli-matol.*, *47*, 525–543.

Mullendore, G. L., D. R. Durran, and J. R. Holton (2005), Cross-tropopause tracer transport in midlatitude convection, *J. Geophys. Res.*, *110*(D06), 113, doi: 10.1029/2004JD005059.

Negri, A. J. (1982), Cloud-top structure of tornado storms on 10 april 1979 from rapid scan and stereo satellite observations, *Bull. Amer. Meteor. Soc.*, *63*, 1851–1859.

Poulida, O., R. R. Dickerson, and A. Heymsfield (1996), Stratosphere-troposphere exchange in a midlatitude mesoscale convective complex, *J. Geophys. Res.*, *101*(D3), 6823–6836.

Ray, E. A., K. H. Rosenlof, E. C. Richard, P. K. Hudson, D. J. Cziczo, M. Loewenstein, H. J. Jost, J. Lopez, B. Ridley, A. Weinheimer, D. Montzka, D. Knapp, S. C. Wofsy, B. C. Daube, C. Gerbig, I. Xueref, and R. L. Herman (2004), Evidence of the effect of summertime midlatitude convection on the subtropical lower stratosphere from CRYSTAL-FACE tracer measurments, *J. Geophys. Res.*, *109*(D18), 304, doi:10.1029/2004JD004655.

Rosenfeld, D., W. L. Woodley, A. Lerner, G. Kelman, and D. T. Lindsey (2008), Satellite detection of severe convective storms by their retrieved vertical profiles of cloud particle effective radius and thermodynamic phase, *J. Geophys. Res.*, *113*(D04), 208, doi:10.1029/2007JD008600.

Schmetz, J., S. A. Tjemkes, M. Gube, and L. van de Berg (1997), Monitoring deep convection and convective overshooting with METEOSAT, *adv. Space Res.*, *19*, 433–441.

Setvak, M., R. M. Rabin, and P. K. Wang (2007), Contribution of the MODIS instrument to observations of deep convective storms and stratospheric moisture detection in GOES and MSG imagery, *Atmos. Res.*, *83*, 505–518.

Setvàk, M., K. Bedka, D. T. Lindsey, A. Sokol, Z. Charvát, J. Štástka, and P. K. Wang (2013), 2013: A-Train observations of deep convective storm tops, *Atmos. Res.*, *123*, 229–248, doi:10.1016/j.atmosres.2012.06.020.

Stohl, A., H. Wernli, P. James, M. Bourqui, C. Forster, M. A. Liniger, P. Seibert, and M. Sprenger (2003), A new perspective of stratosphere-troposphere exchange, *Bull. Amer. Meteor. Soc.*, *84*, 1565–1573.

Wang, P. K. (2003), Moisture plumes above thunderstorm anvils and their contributions to cross-tropopause transport of water vapor in midlatitudes, *J. Geophys. Res.*, *108*(D6), 4194, doi:10.1029/2002JD002581.

WMO (1957), Meteorology - a three-dimensional science: Second session of the commision for aerology, *WMO Bulletin*, *IV*(4), 134–138.

Wong, S., and W.-C. Wang (2000), Interhemispheric asymmetry in the seasonal variation of the zonal mean tropopause, *J. Geophys. Res.*, *105*(D21), 26,645–26,659.